Role of surface oxidation in enhancing heat transfer across graphene-water interface via Thermal Boundary Resistance modulation (Supporting Information)

Fabiano Tarulli[1,2,*], Francesco Maria Bellussi[1,3,*], Marina Provenzano[1], Paolo De Angelis[1], Alessandro Casto[2], Margherita Vittucci[2], Natalia Del Fatti[2,4], Francesco Banfi[2], Paolo Maioli[2], and Matteo Fasano[1,**]

[1] Department of Energy "Galileo Ferraris", Politecnico di Torino, Corso Duca degli Abruzzi, 24, Turin, 10129, Italy

[2] FemtoNanoOptics group, Université de Lyon, CNRS, Université Claude Bernard Lyon 1, Institut Lumière Matière, F-69622, Villeurbanne, France

[3] Empa, Swiss Federal Laboratories for Materials Science and Technology, Chemical Energy Carriers and Vehicle Systems Laboratory, 8600 Dübendorf, Switzerland

[4] Institut Universitaire de France (IUF), France

[*] These authors contributed equally to the work

[**] Corresponding author: matteo.fasano@polito.it

S1 Details of the models developed

The details of the developed models are reported in Table S1. The parameters of the force fields adopted for graphene, hydroxyl groups, and water molecule are summarized in Tables S2 and S3.

Table S1: Characteristics of the various simulated systems

Oxidation degree	# of hydroxyl groups	# of carbon atoms (graphene)	# of water molecules
0%	0	1972	25392
5%	99	1972	25392
10%	197	1972	25392
20%	394	1972	25392
40%	789	1972	25392
60%	1183	1972	25392
80%	1578	1972	25392

Atom types:

O ⟶ Oxygen atom of water molecule
H ⟶ Hydrogen atom of water molecule
C ⟶ Carbon atom of graphene not bonded to any functional group
C_f ⟶ Carbon atom of graphene bonded to a functional group
O_f ⟶ Oxygen atom in functional group
H_f ⟶ Hydrogen atom in functional group

S1.1 Bonded interactions

Bond stretching:

Potential energy V_B of a chemical bond as a function of the distance r between two atoms:

$$V_B(r) = K_2(r - r_0)^2 + K_3(r - r_0)^3 + K_4(r - r_0)^4,$$

where r_0 represents the equilibrium bond length.

Angle bending:

Potential energy V_A associated with the variation of the angle θ between three atoms connected by chemical bonds:

$$V_A(\theta) = L_2(\theta - \theta_0)^2 + L_3(\theta - \theta_0)^3 + L_4(\theta - \theta_0)^4,$$

where θ_0 represents the equilibrium bond angle.

Table S2: Force field parameters for bonded interactions (2 and 3 bodies)

Type	$\mathbf{r_0}$ (Å)	$\mathbf{K_2}$ (kcal/mol/Å^2)	$\mathbf{K_3}$ (kcal/mol/Å^3)	$\mathbf{K_4}$ (kcal/mol/Å^4)
OH	0.9572	552.0	-1276.0	1787.0
C_fO_f	1.3768	428.8798	-738.2351	1114.9655
O_fH_f	0.9494	540.3633	-1311.8663	2132.4446
Type	θ_0 (°)	$\mathbf{L_2}$ (kcal/mol/rad^2)	$\mathbf{L_3}$ (kcal/mol/rad^3)	$\mathbf{L_4}$ (kcal/mol/rad^4)
HOH	104.52	46.65	-11.7	-8.79
$C_fO_fH_f$	108.19	53.1250	-8.5016	0.0

S1.2 Non-bonded interactions

Lennard-Jones 9-6 potential equation:

$$V_{\text{LJ-9-6}}(r) = \varepsilon \left[2 \left(\frac{\sigma}{r} \right)^9 - 3 \left(\frac{\sigma}{r} \right)^6 \right].$$

Table S3: Lennard-Jones 9-6 parameters for non-bonded interactions

Type	ε **(kcal/mol)**	σ **(Å)**
O-O	0.08	3.84
H-H	0.008	1.087
C-C	0.0	0.0
C_f-C_f	0.0	0.0
O_f-O_f	0.0960	3.5800
H_f-H_f	0.0080	1.0870
O-H	0.00114707	3.42134
O-C	0.0736323	3.87841
O-C_f	0.0736323	3.87841
O-O_f	0.0857323	3.72132
O-H_f	0.00114707	3.42134
H-C	0.000997985	3.48813
H-C_f	0.000997985	3.48813
H-O_f	0.00155028	3.18983
H-H_f	0.0080	1.087
C-C_f	0.0	0.0
C-O_f	0.0779716	3.76602
C-H_f	0.000997985	3.48813
C_f-O_f	0.0779716	3.76602
C_f-H_f	0.000997985	3.48813
O_f-H_f	0.00155028	3.18983

Further details:

Carbon atom interactions are handled by the TERSOFF forcefield [1]; therefore, the associated σ and ϵ values in Table S3 are set to zero. All other bonded and non-bonded interaction parameters listed above, including those in Tables S2 and S3, correspond to the COMPASS forcefield [2], which was used to model water molecules, hydroxyl groups, and their interactions with graphene.

ϵ and σ for interactions between different atom types are calculated through Lorentz-Berthelot rules: $\sigma_{ij} = \frac{\sigma_{ii}+\sigma_{jj}}{2}$ and $\epsilon_{ij} = \sqrt{\epsilon_{ii}\epsilon_{jj}}$.

S2 Summary of the setup

In Figure S1 are shown snapshots of the MD setup.

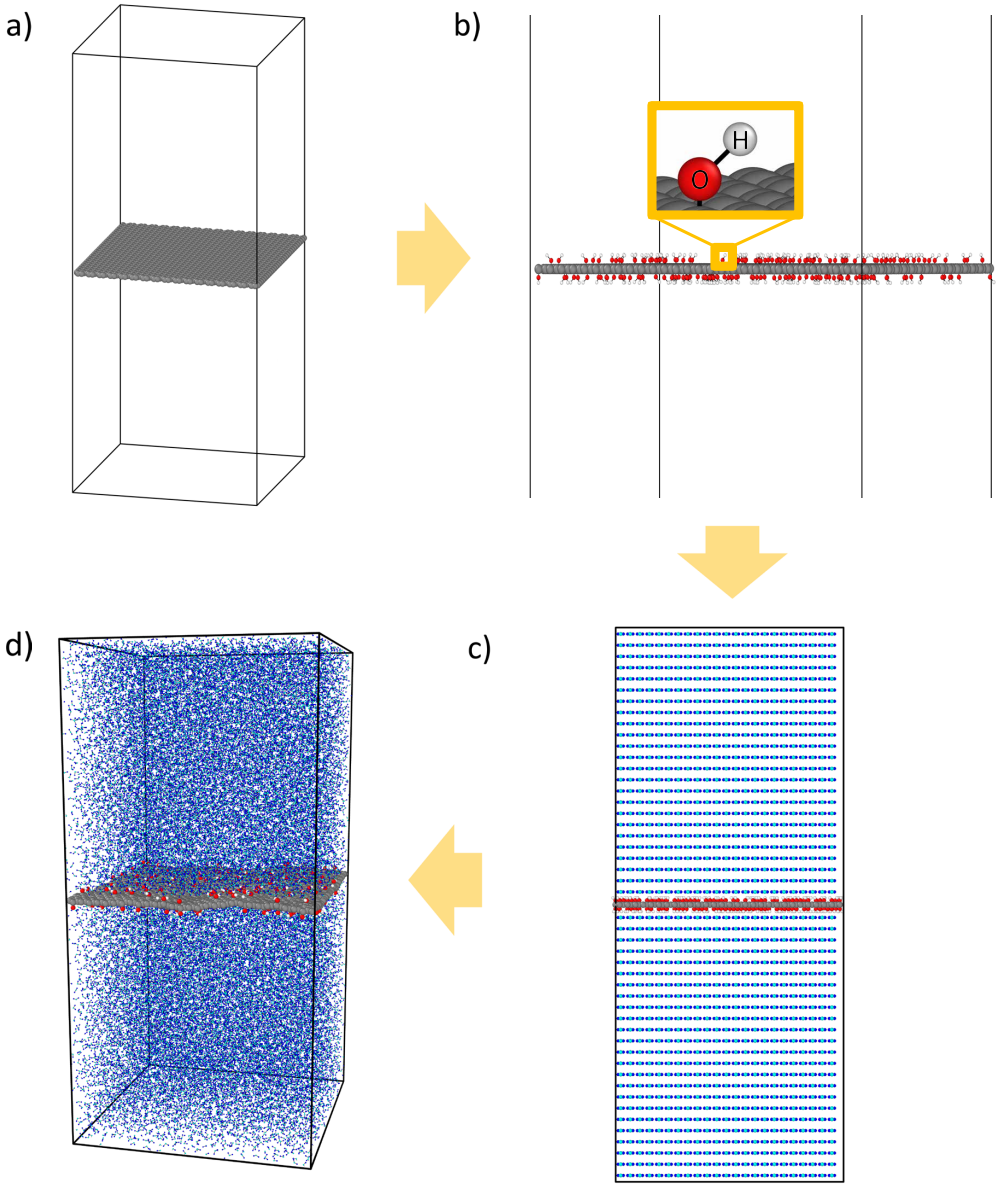

Figure S1: (a) Pristine graphene centered within the simulation box. (b) Introduction of hydroxyl functional groups (-OH) onto the graphene surface. (c) Addition of water molecules, representing the initial configuration of the simulation system. (d) Snapshot of the system during the NVE ensemble simulation, showing interactions between the functionalized graphene and the surrounding water molecules.
(Simulation box height: ~ 15.2 nm; cross-sectional area: $\sim 7.2 \times 7.2\,\mathrm{nm}^2$.)

S3 Computation of the thermal boundary resistance

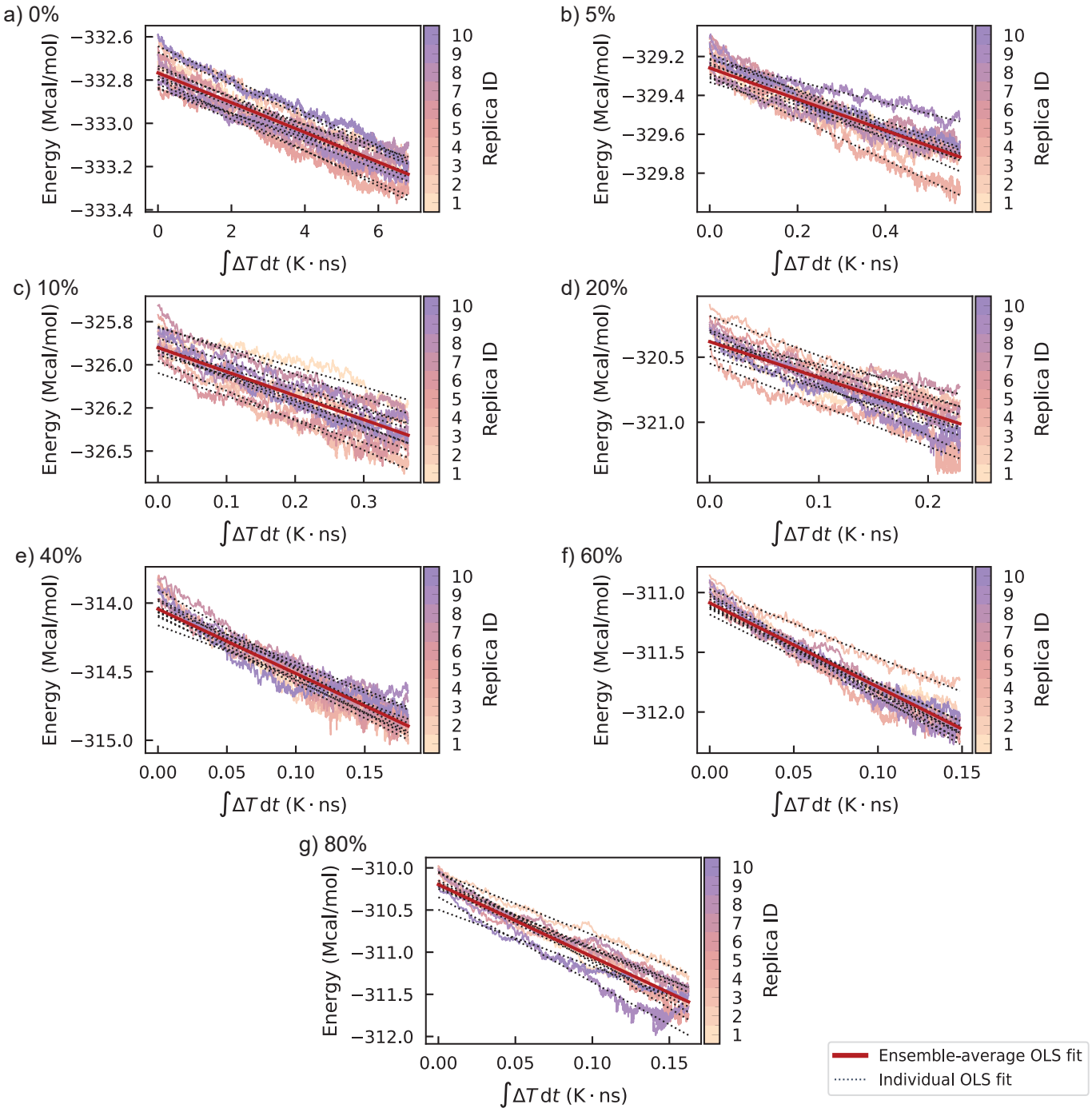

Figure S2: Panels a) to g) correspond to all simulated systems, each representing a distinct hydroxyl group coverage on the graphene surface. The horizontal axes show the time-integrated temperature difference between graphene and water. The vertical axes show the evolution of graphene's total energy. Each panel displays ten independent approach-to-equilibrium MD replicas, colour-coded by replica ID (colour bar on the right). Black dotted lines represent ordinary least squares (OLS) fits applied to each replica, with the fitting range determined by an iterative algorithm that identifies the linear interval. The red solid line represents the ensemble-average OLS fit, built from the average slope and intercept of the individual replica fits. Only data within the linear interval are shown.

The thermal boundary resistance is calculated following Jabbari et al. [3]. From energy conservation applied to graphene (Eq. S1), the integral of the temperature difference $\int_0^{\mathrm{t}} (\mathrm{T_p(t)} - \mathrm{T_a(t)})\,\mathrm{dt}'$ is treated as the independent variable. The total graphene energy E(t) is then approximated as linear during heat exchange, and the slope, adjusted for the heat exchange area S, yields the $\mathrm{R_K}$ value.

$$\frac{\partial E(t)}{\partial t} = -\frac{T_p(t) - T_a(t)}{R_K/S} \qquad \xrightarrow{\text{integrating}} \qquad E(t) = E_0 - \frac{S}{R_K}\int_0^t \left[T_p(t') - T_a(t')\right] dt' \tag{S1}$$

The procedure was applied to each individual replica, and the average slope was then calculated to obtain the $\mathrm{R_K}$ value corresponding to each oxidation level (see Algorithm 1). The uncertainty in the average slope, estimated using the standard error across replicas, was propagated to the Kapitza resistance using the error propagation method. The following paragraph describes the critical procedure used to post-process the trajectory and to obtain the linear trend required by the approach-to-equilibrium method.

The overall fitting procedure to extract the interfacial thermal conductance $G_k(\theta_{OX})$ from molecular dynamics is summarized in the main routine (Algorithm 1). For each oxidation level θ_{OX} and for each replica i, we first construct the driving and response signals: the instantaneous temperature difference between the graphene oxide sheet and the adjacent liquid, $\Delta T(t,i) = T_{\mathrm{p}}(t,i) - T_{\mathrm{a}}(t,i)$, is integrated in time to obtain a cumulative thermal driving term $I'(t,i)$:

$$I'(t,i) = I(t,i) - I(t_{\mathrm{start}},i) \quad \text{where} \quad I(t,i) = \int \Delta T(t,i)\,dt.$$

This step is implemented in BuildCumulative (Algorithm 2), which applies a trapezoidal time integration and shifts the result so that $I'(t_{\mathrm{start}},i) = 0$. We then pair $I'(t,i)$ with the total energy of the solid region, $E_{\mathrm{tot}}(t,i)$, and identify the time window in which the system exhibits linear response. Specifically, for each replica we detect a breakpoint $t_0(i)$ using FindBreak (Algorithm 3), which scans candidate break times and selects the one that best separates an early linear regime (energy changing approximately linearly with I') from a later plateau regime (energy nearly constant). In theory, according to Jabbari et al. [3], this integral should vanish at long times and therefore should not affect the fit. In practice, however, this behavior does not occur; instead, a plateau develops because the thermal fluctuations become comparable to (and eventually dominate over) the residual temperature difference, which is on average zero, and this produces a non-zero value of the time integral. For this reason, the FindBreak automatic procedure to identify and exclude the noisy and steady-state regime is required.

The global fitting interval is taken as $t < t_0^*(\theta_{OX}) = \min_i t_0(i)$, so that all replicas are subsequently fit over the same strictly linear window. Within this common window, FitSlope (Algorithm 4) performs an ordinary least-squares regression for each replica,

$$E_{\mathrm{tot}}(t,i) \approx a_i + m_i\, I'(t,i),$$

and returns the replica slope m_i. The per-replica slopes are then fed to AggregateSlopes (Algorithm 5), which computes the mean slope $\bar{m}(\theta_{OX})$ and its 95% confidence interval error, using the two-tailed Student's t-distribution with $(N_{\mathrm{rep}} - 1)$ degrees of freedom. Finally, SlopeToGK (Algorithm 6) converts $\bar{m}(\theta_{OX})$ into the interfacial Kapitza resistance

$$R_k(\theta_{OX}) = -\frac{A(\theta_{OX})}{\bar{m}(\theta_{OX})},$$

using the simulated contact area $A(\theta_{OX})$, and then reports the interfacial conductance as $G_k(\theta_{OX}) = 1/R_k(\theta_{OX})$ together with its propagated uncertainty.

The full in-house python code is available online at the web address `https://github.com/Fabber12/water-graphene_oxide`.

Algorithm 1 Main routine: Interfacial conductance $G_k(\theta_{OX})$ extraction

Require: For each oxidation level θ_{OX} and replica i: $T_{\mathrm{p}}(t,i)$, $T_{\mathrm{a}}(t,i)$, $E_{\mathrm{tot}}(t,i)$, and interfacial area $A(\theta_{OX})$.

1. Build signals
for each i **do**
    $\Delta T(t,i) \leftarrow T_{\mathrm{p}}(t,i) - T_{\mathrm{a}}(t,i)$
    $I'(t,i) \leftarrow \textsc{BuildCumulative}\big(\Delta T(t,i)\big)$
end for
2. Determine linear window
for each i **do**
    $t_0(i) \leftarrow \textsc{FindBreak}\big(I'(t,i), E_{\mathrm{tot}}(t,i)\big)$
end for
$t_0^*(\theta_{OX}) \leftarrow \min_i t_0(i)$
3. Fit per-replica slopes
for each i **do**
    $m_i \leftarrow \textsc{FitSlope}\big(I'(t,i), E_{\mathrm{tot}}(t,i), t_0^*(\theta_{OX})\big)$
end for
$\bar{m}(\theta_{OX}), \sigma_{\bar{m}}(\theta_{OX}) \leftarrow \textsc{AggregateSlopes}\big(\{m_i\}_i\big)$
4. Convert slope to R_k and G_k
$R_k(\theta_{OX}), \Delta R_k(\theta_{OX}), G_k(\theta_{OX}), \Delta G_k(\theta_{OX}) \leftarrow \textsc{SlopeToGK}\big(\bar{m}(\theta_{OX}), \sigma_{\bar{m}}(\theta_{OX}), A(\theta_{OX})\big)$
return $G_k(\theta_{OX}) \pm \Delta G_k(\theta_{OX})$

Algorithm 2 Subroutine BuildCumulative

Require: Temperature difference $\Delta T(t_k, i)$ at discrete time steps t_k.

Smooth thermal noise using a W-point moving average:

$$\Delta T(t_k, i) \leftarrow \frac{1}{W} \sum_{j=0}^{W-1} \Delta T(t_{k-j}, i)$$

Compute cumulative integral via trapezoidal rule:

$$I(t,i) = \int \Delta T(t,i)\, dt$$

Shift so it starts at zero:

$$I'(t,i) = I(t,i) - I(t_{\mathrm{start}}, i)$$

return $I'(t,i)$

Algorithm 3 Subroutine FindBreak

Require: $I'(t,i)$ and $E_{\mathrm{tot}}(t,i)$ for one replica i.

for each trial breakpoint t_0 on a scan grid **do**
    Pre-break set $\mathcal{S}_{\mathrm{lin}} = \{t < t_0\}$, post-break set $\mathcal{S}_{\mathrm{plat}} = \{t \geq t_0\}$
    Fit $E_{\mathrm{tot}} = a + m\, I'$ on $\mathcal{S}_{\mathrm{lin}}$ (OLS)
    Fit $E_{\mathrm{tot}} = c$ on $\mathcal{S}_{\mathrm{plat}}$ (constant fit)
    Compute cost:

$$\mathrm{err}(t_0) = \mathrm{MSE}_{\mathrm{lin}} + \lambda\, \mathrm{MSE}_{\mathrm{plat}} + \mathrm{penalty(short\ segment)}$$

end for
$t_0(i) \leftarrow \arg\min_{t_0} \mathrm{err}(t_0)$
return $t_0(i)$

Algorithm 4 Subroutine FitSlope

Require: $I'(t,i)$, $E_{\mathrm{tot}}(t,i)$, and global cutoff $t_0^*(\theta_{OX})$.

1: Keep only samples with $t < t_0^*(\theta_{OX})$.

2: Perform OLS fit:

$$E_{\mathrm{tot}}(t,i) \approx a_i + m_i\, I'(t,i)$$

3: **return** m_i

Algorithm 5 Subroutine AggregateSlopes

Require: Slopes $\{m_i\}_{i=1}^{N_{\mathrm{rep}}}$.

1: $\bar{m} = \dfrac{1}{N_{\mathrm{rep}}} \sum_i m_i$

2: Determine the 95% confidence factor $t_{0.975,\,N_{\mathrm{rep}}-1}$ (Student's t-distribution)

3: $\sigma_{\bar{m}} = t_{0.975,\,N_{\mathrm{rep}}-1} \times \dfrac{\mathrm{std}(m_i)}{\sqrt{N_{\mathrm{rep}}}}$ (95% CI)

4: **return** $\bar{m}, \sigma_{\bar{m}}$

Algorithm 6 Subroutine SlopeToGK

Require: $\bar{m}(\theta_{OX})$, $\sigma_{\bar{m}}(\theta_{OX})$, $A(\theta_{OX})$, Avogadro N_A.

1: Compute Kapitza resistance:

$$R_k(\theta_{OX}) = -\frac{A(\theta_{OX})}{\bar{m}(\theta_{OX})}$$

2: Propagate its uncertainty:

$$\Delta R_k(\theta_{OX}) = \frac{A(\theta_{OX})}{\bar{m}(\theta_{OX})^2}\, \sigma_{\bar{m}}(\theta_{OX})$$

3: Then thermal conductance:

$$G_k(\theta_{OX}) = \frac{1}{R_k(\theta_{OX})}, \qquad \Delta G_k(\theta_{OX}) = \frac{\Delta R_k(\theta_{OX})}{R_k(\theta_{OX})^2}$$

4: **return** $R_k(\theta_{OX}), \Delta R_k(\theta_{OX}), G_k(\theta_{OX}), \Delta G_k(\theta_{OX})$

S4 Effect of different graphene initial temperature on thermal boundary resistance

We evaluated the sensitivity of the AEMD-derived Kapitza resistance to the initial graphene–water temperature difference. Two oxidation levels were considered: pristine graphene and 40% hydroxyl-functionalized graphene. For each oxidation degree, six temperature offsets were tested by setting the initial graphene temperature to 330, 340, 350, 360 (reference case), 370, and 380 K, while keeping the water fixed at 298 K. The minimum temperature difference was chosen to ensure that it exceeded the intrinsic thermal fluctuations, allowing a clear distinction between random noise and the imposed temperature gradient. Five independent replicas were performed for each condition. The Kapitza resistance R_K and its relative standard error were extracted following the analysis protocol described in Section S3, using a 9 Å thick water slab as the reference case. Within the statistical uncertainty, R_K shows no appreciable variation over the explored temperature range, indicating that the AEMD-derived TBR is only marginally influenced by the imposed thermal gradient.

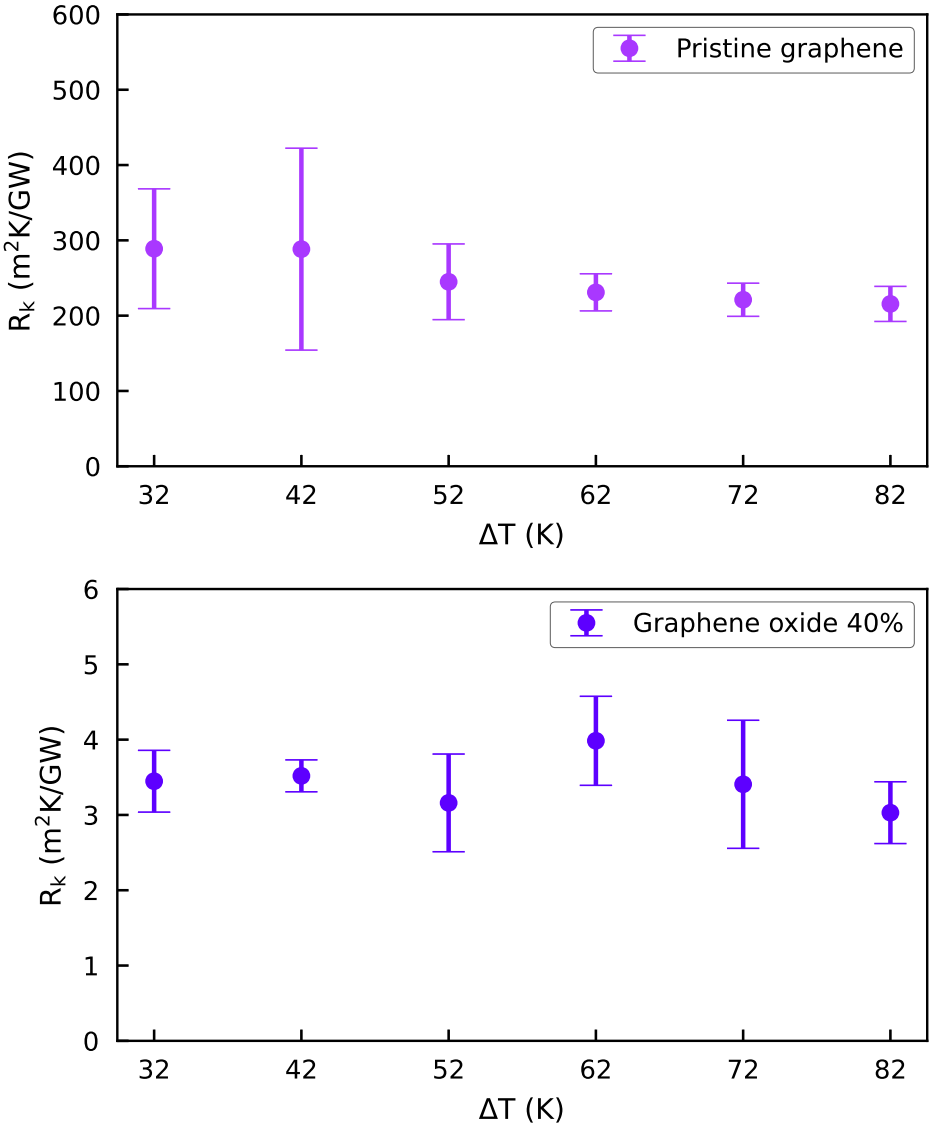

Figure S3: Dependence of the Kapitza resistance R_K on the initial temperature difference $\Delta T = T_{p,0} - T_{a,0}$ between water and pristine graphene or 40% graphene oxide. Each point represents the average of five replicas, with error bars indicating the relative standard error.

S5 Density profiles

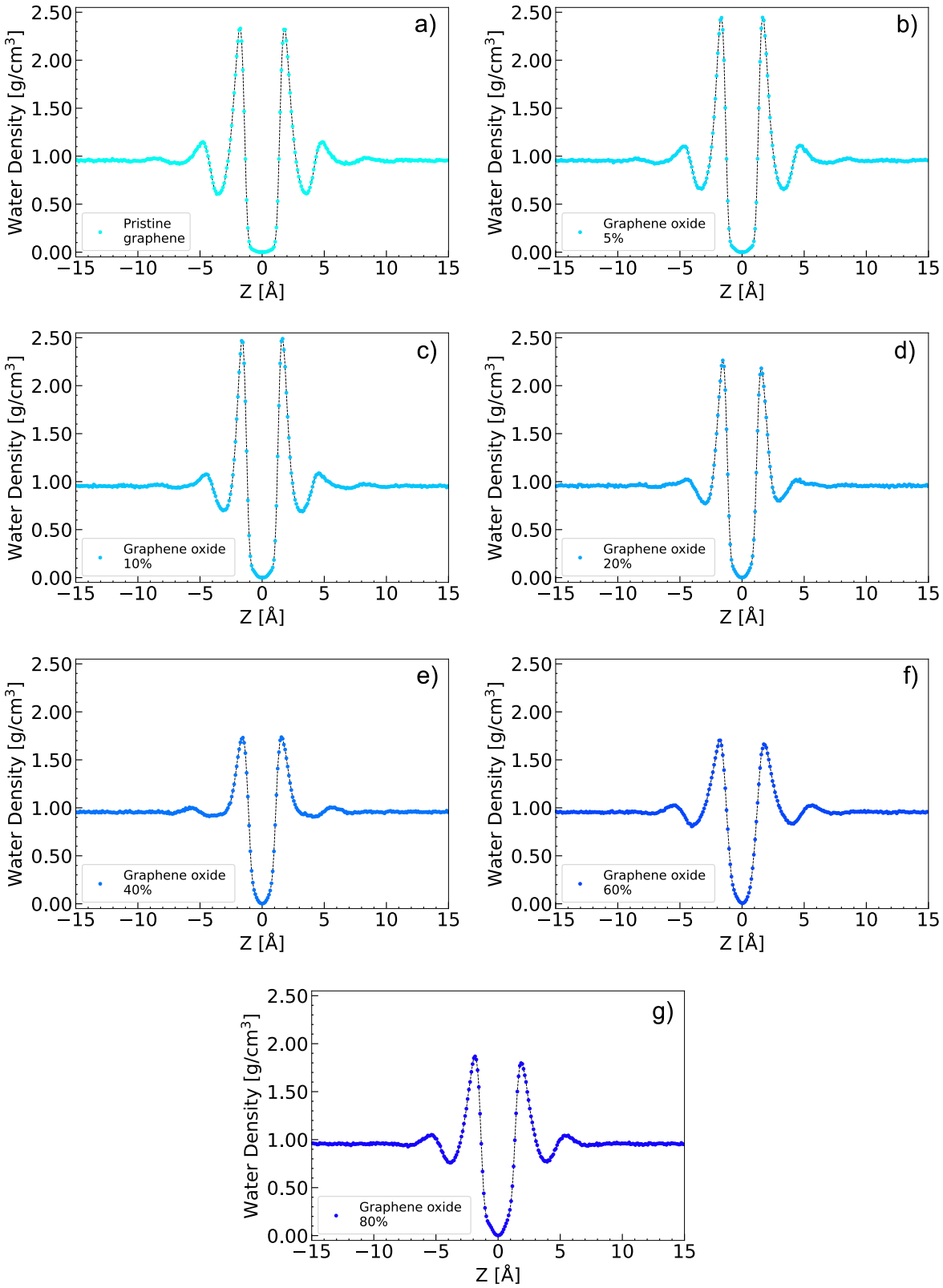

Figure S4: Water density profiles for different systems with graphene at varying oxidation levels, ranging from 0% (pristine graphene) in panel (a) to 80% in panel (g). The dots represent the computed density, while the dashed curves are obtained using Cubic Hermite interpolation.

The thickness of the interfacial water layer was determined to track the time-dependent temperature $T_a(t)$ and, in turn, calculate the Kapitza resistance R_K. We obtained this thickness by averaging the z-coordinates (normal to graphene surface) of the water particles in the bin corresponding to the local minimum immediately after the second peak in Figure S4 (see Section S6). This procedure yields a uniform slab thickness of 9 Å for all systems. Due to the symmetry of the model, the same interfacial layer was considered above and below the graphene sheet, i.e., $T_a\big(t,\ -9\,\text{Å} \leq Z \leq 9\,\text{Å}\big)$.

S6 Effect of different layer widths on thermal boundary resistance

In the systems with low oxidation degrees, the TBR remains largely insensitive to the chosen thickness of the interfacial water slab. This is reflected by the consistent values of R_K obtained across different slab thicknesses, with uncertainties overlapping for all oxidation degrees up to 40%, as shown in Figure S5. Starting from 40% hydroxyl coverage, however, a slight deviation appears: R_K shows a mild dependence on the liquid-layer thickness used to compute the interfacial temperature. This behaviour is physically reasonable, as high hydroxyl densities promote stronger and more directional hydrogen bonding between surface –OH groups and nearby water molecules. These interactions enhance water structuring and slow down local relaxation dynamics in the first hydration layers, leading to a more pronounced temperature gradient within the interfacial region. As a result, the TBR becomes slightly more sensitive to the precise definition of the interfacial slab. TBR at solid–liquid interfaces primarily arises within the first nanometer of interfacial water, where structural ordering and vibrational coupling to the solid surface govern heat transfer. Don *et al.* [4] showed that structural and dynamical perturbations of interfacial water decay within approximately 1 nm from the graphene oxide surface, with the first confined layer exhibiting distinct density and orientation features. These results justify defining the thermally coupled interfacial-water region—and thus the TBR evaluation zone—as about 1 nm thick. Accordingly, a slab thickness of 9 Å, representing the first minimum after the second peak of the water density profile, was adopted for all TBR evaluations in this work.

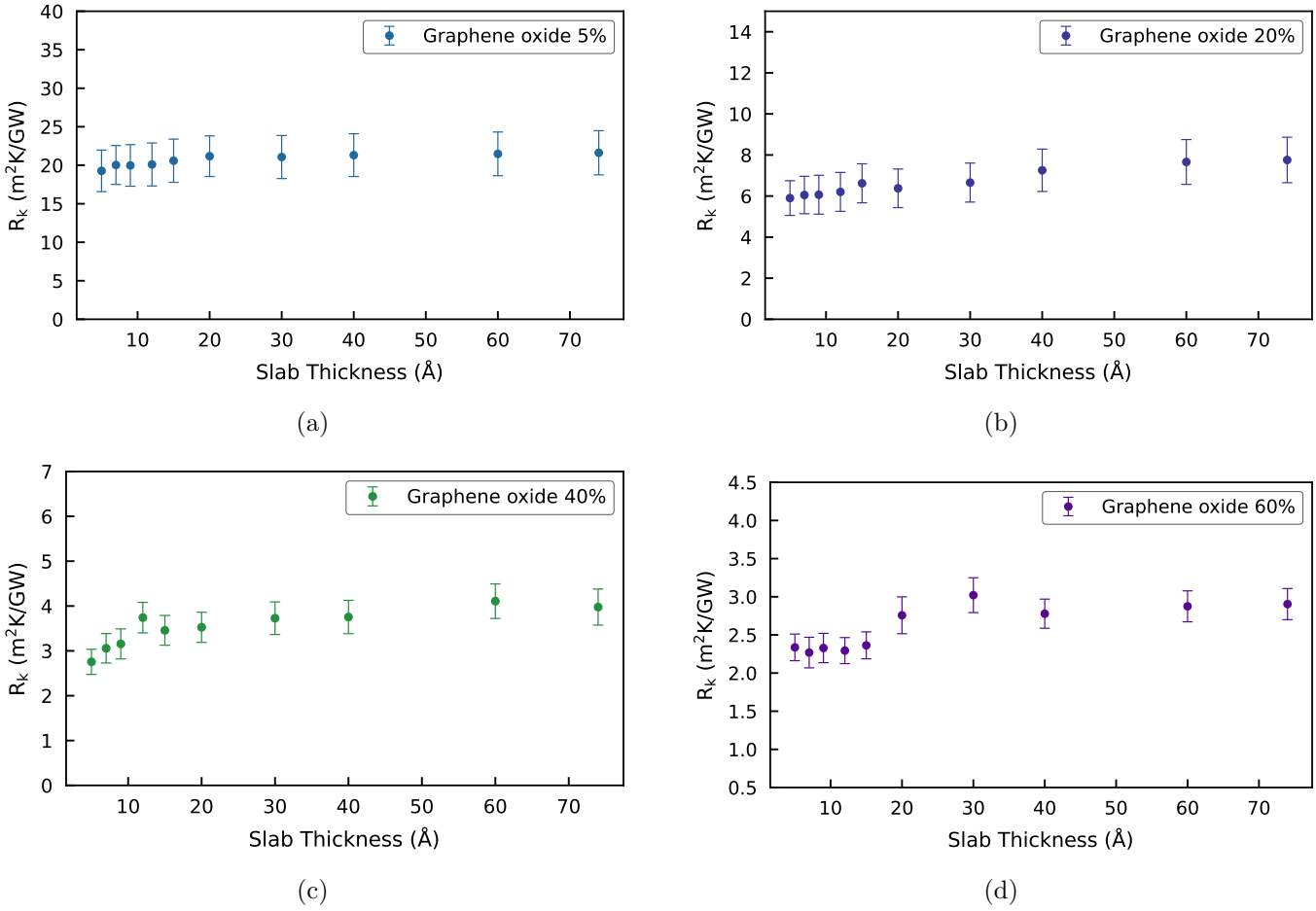

Figure S5: Thermal boundary resistance (R_K) for graphene oxide with (a) 5%, (b) 20%, (c) 40%, and (d) 60% oxidation as a function of different slab thicknesses, within which the water temperature was evaluated. Data points represent simulation results, and error bars indicate the uncertainty for each measurement. The last data point on the right corresponds to the TBR calculated using the bulk temperature.

S7 Phonon overlap analysis

Phonon overlap rate S between graphene and interfacial water was computed to assess interfacial vibrational matching, following Yang *et al.* [5]:

$$S = \int \omega f(\omega) d\omega, \tag{S2}$$

where ω is the vibrational frequency, and $f(\omega)$ represents the cross-over overlap area of the phonons with frequency ω. For each oxidation degree, three independent simulations were performed. The phonon density of states (PDOS) of both graphene and interfacial water were obtained from the discrete cosine transform (DCT) of the velocity autocorrelation functions (VACF), averaged over 400 microcanonical (NVE) windows of 2.5 ps each. To capture the dynamics of interfacial water, molecules located within 9 Å above and below the graphene sheet were identified at the beginning of each window, and their velocities were tracked over time following a Lagrangian approach. A check on molecular displacements at the slab boundaries confirmed that, within each 2.5 ps window, water molecules leaving the interfacial region do not travel far from it, ensuring the validity of the instantaneous interfacial definition. However, we observed that increasing the assumed thickness of the interfacial layer, up to and including a bulk-like limit, does not affect S. The overlap factor quantifies the degree of vibrational mode matching across the interface, with higher values indicating stronger phonon coupling and enhanced thermal transport. While S generally increases with hydroxyl coverage, its apparent linearity tends to weaken at high oxidation levels, suggesting a possible saturation of vibrational coupling as the interface becomes densely functionalized.

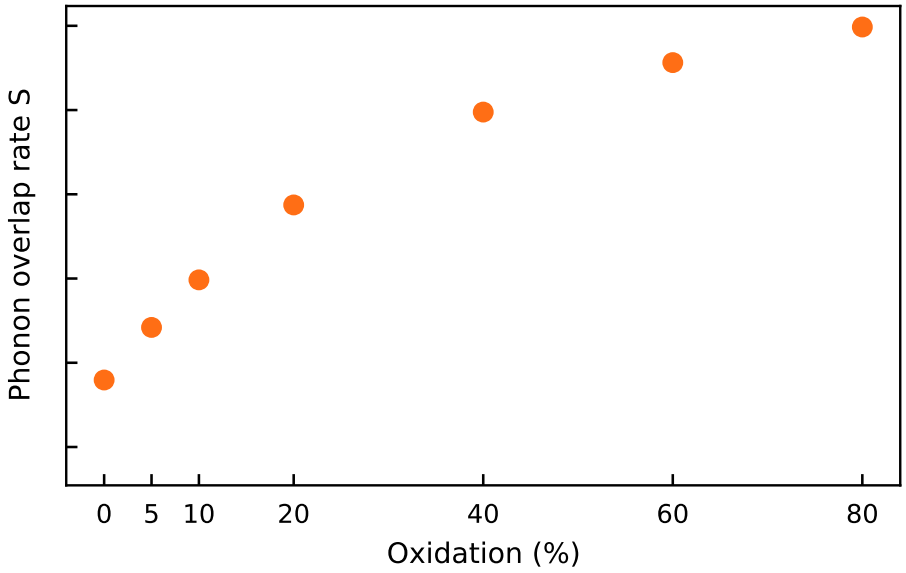

Figure S6: Evolution of the phonon overlap rate S between graphene and interfacial water with increasing oxidation degree. Higher S values indicate stronger vibrational coupling and correlate with the observed decrease in R_K.

S8 Summary of results compared with literature

Table S4: TBR for different oxidation degrees of graphene. Mean values (R_K) and Relative Standard Error (RSE) were derived from 10 simulation replicates per oxidation level.

Oxidation (%)	$\mathbf{R_K}$ ($m^2\,K\,GW^{-1}$)	**RSE** (%)
0	227	9.4
5	20	14
10	11	9.7
20	6.1	16
40	3.2	11
60	2.3	8.3
80	1.9	12

Table S5: Experimental TBR for two graphene oxidation levels [6]. For each quantity, mean values and corresponding standard deviations are provided.

Oxidation (%)	$\mathbf{R_K}$ ($m^2\,K\,GW^{-1}$)
17 ± 1%	23 ± 2
44 ± 2%	13 ± 2

Table S6: Literature-reported TBR values for interfaces between multi-layer pristine graphene and water; N indicates the number of graphene layers.

N	$\mathbf{R_K}$ ($m^2\,K\,GW^{-1}$)	**Water model**	**Author**	**Forcefield**
2	54.61 ± 0.71	SPC/E	Alexeev *et al.* [7]	Hybrid Tersoff
4	43.98 ± 0.66	SPC/E	Alexeev *et al.* [7]	Hybrid Tersoff
8	32.28 ± 1.13	SPC/E	Alexeev *et al.* [7]	Hybrid Tersoff
12	27.03 ± 1.10	SPC/E	Alexeev *et al.* [7]	Hybrid Tersoff
10	12.75 ± 0.50	SPC	Alosius *et al.* [8]	Hybrid Tersoff

Table S7: TBC and relative standard error (RSE) for graphene at different oxidation levels. TBC is calculated as the reciprocal of the Kapitza resistance R_K.

Oxidation (%)	$\mathbf{1/R_K}$ ($MW\,m^{-2}\,K^{-1}$)	**RSE** (%)
0	4.4	9.4
5	50	14
10	87	9.7
20	165	16
40	317	11
60	430	8.3
80	520	12

S9 Linear model for predicting oxidation degree

The MD results show a linear increase of $1/R_K$ with oxidation degree over the range 0–60%, with a slight deviation from linearity approaching higher oxidation coverages, as discussed in the main text. The MD regression yields the following coefficients:

$$b_{\mathrm{MD}} = 14 \pm 8 \tag{S3}$$

$$m_{\mathrm{MD}} = 7.1 \pm 0.2 \tag{S4}$$

where b_{MD} is the intercept and m_{MD} is the slope, both expressed in $\mathrm{MW\,m^{-2}\,K^{-1}}$. An R-squared = 0.995 confirms that the linear model captures almost all the variance in the MD data. Although the experimental study provides only two oxidation levels and therefore cannot independently resolve a full regression, the experimentally observed increase in conductance is consistent with the monotonic trend obtained in MD. The MD regression can also be inverted to estimate the corresponding oxidation degree:

$$\alpha = \frac{G - b_{\mathrm{MD}}}{m_{\mathrm{MD}}},$$

where α represents the hydroxyl coverage, and its uncertainty is calculated by propagating the errors of the fitted parameters. The MD regression is consistent with the experimental trend reported in [6], but it cannot be used to infer experimental oxidation levels because real systems contain mixed functional groups, defects, and hydration structures not represented in the hydroxyl-only MD models. Thus, the linear relation obtained here should be viewed as internally coherent within the MD framework, not as a quantitative predictor for experimental samples.

S10 Roughness analysis

For each oxidation degree, three independent simulations were performed, and the structural roughness of the graphene/graphene-oxide sheet was quantified directly from the molecular dynamics trajectories. The instantaneous interface was defined from the positions of the carbon atoms in the sheet; for every stored configuration, we determined a best-fit reference plane and measured the out-of-plane height fluctuations relative to it. From the resulting height distributions, we extracted a scalar measure of the corrugation amplitude and evaluated the Wenzel roughness factor $r = A_{\mathrm{MS}}/A_{\mathrm{proj}}$, where A_{MS} is the molecular surface used to compute the density profile (see Section S5) and A_{proj} is its projection onto the graphene plane. As shown in Fig. S7, the increase in r becomes less pronounced at the highest coverages, and even shows a slight reduction at 80% oxidation.

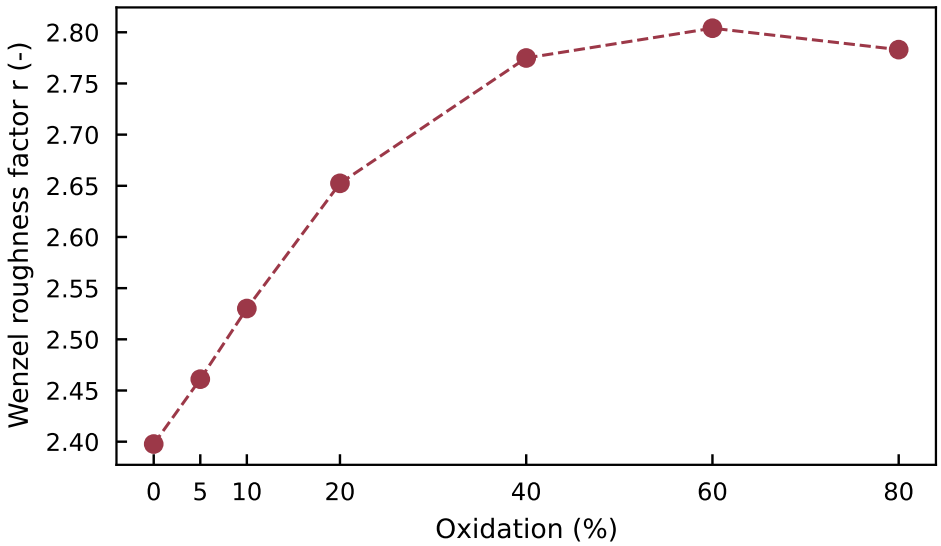

Figure S7: Wenzel roughness factor r of graphene oxide as a function of the oxidation degree. Values extracted from equilibrium molecular dynamics trajectories.

S11 Influence of Wettability on interfacial water layering and Thermal Boundary Resistance

To compare the response of our model with previous ones in the literature, we investigated how the water density peak and the TBR at the pristine graphene interface vary by modifying the system's wettability. For the sake of simplicity, this was achieved by tuning the Lennard-Jones well depth ϵ. The results demonstrate that higher ϵ lead to higher wettability (lower CA), which corresponds to a more pronounced density peak in the water density profiles, consistent with the trend reported in [7].

The TBR values, obtained using the methodology described in this paper and following [3], are presented in

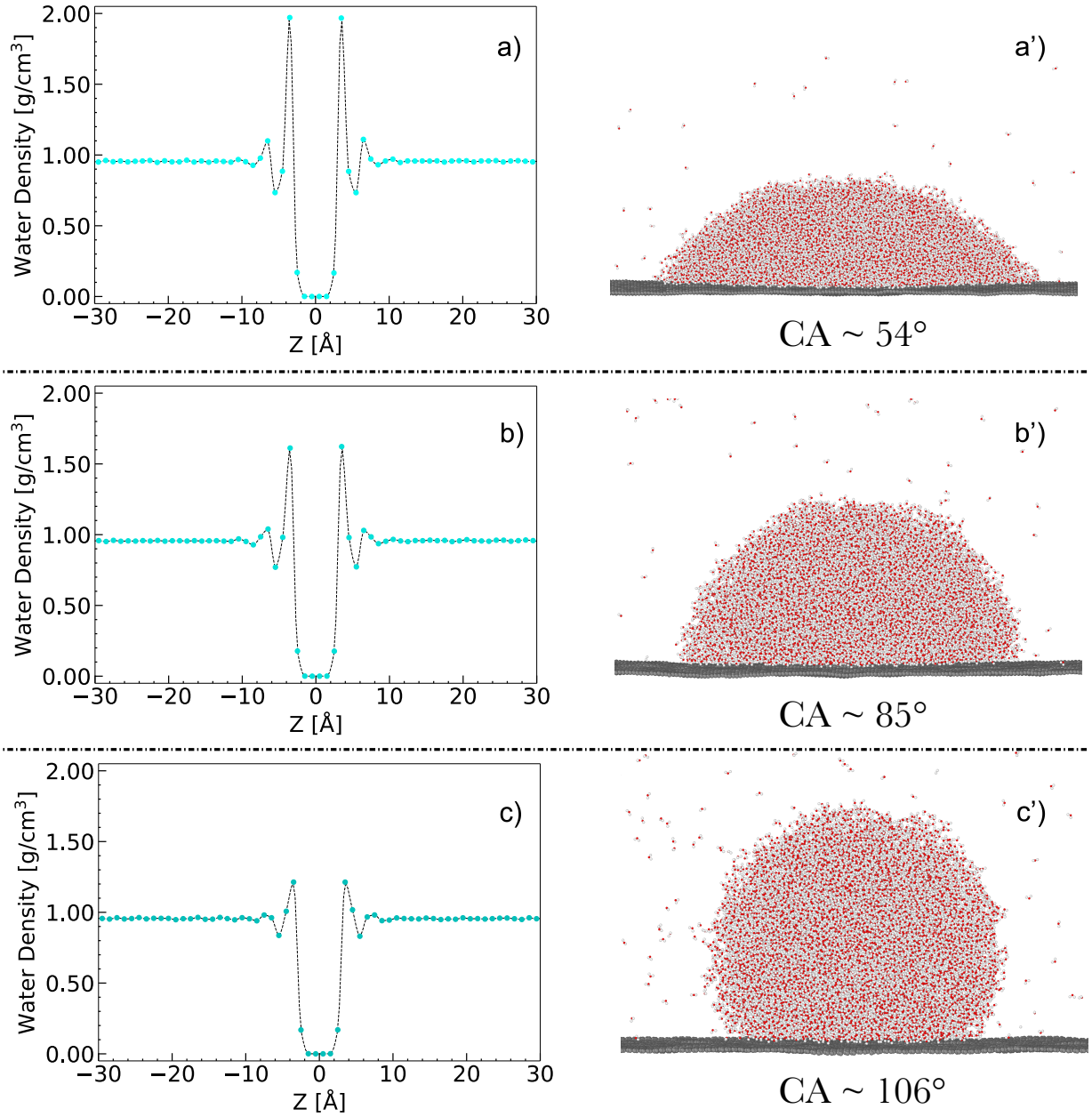

Figure S8: Plots (a, b, c) on the left display the water density profiles at the pristine graphene interface for systems simulated with different Lennard-Jones well depths ϵ (in kcal/mol), representing the interaction between graphene (carbon) and water (oxygen): 0.0736323 (a), 0.05 (b), and 0.03 (c). These variations in ϵ directly influence the graphene surface's wettability, as reflected by the contact angles (CA) measured from water droplet simulations on graphene, shown on the right (a', b', c'). The dots represent the computed density, while the continuous curves are generated using a Cubic Hermite interpolation.

Table S8, again confirming that higher CA values are associated with TBR increase.

CA	$\mathbf{R_K}$ $(\mathrm{m^2\,K\,GW^{-1}})$
$\sim 54^\circ$	237
$\sim 85^\circ$	254
$\sim 106^\circ$	317

Table S8: Kapitza resistance values associated with different contact angles (CA), achieved by varying the Lennard-Jones well depth (ϵ) between carbon atoms in graphene and oxygen atoms in water, as discussed in [7].

S12 Influence of Lennard-Jones well depth on water layering at graphene oxide interface

The hydroxyl groups on the graphene sheet promote complete wetting by water. We then examined the behavior of the water density peak as a function of the Lennard-Jones well depth (ϵ), which is no longer directly linked to a contact angle. The results are consistent with those observed for pristine graphene, with a higher ϵ being responsible for higher water density peaks in the proximity of the solid surface, as detailed in Section S11.

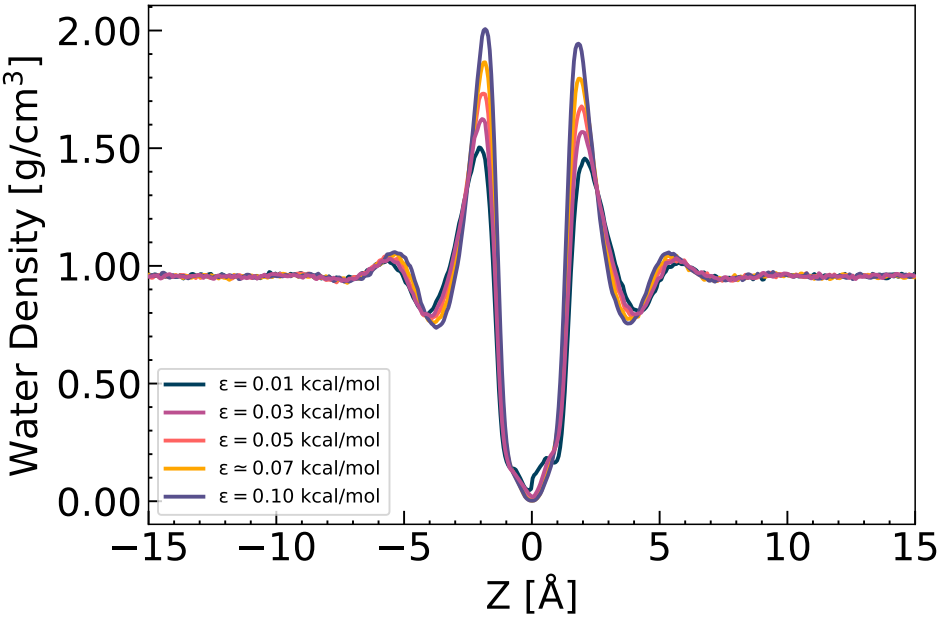

Figure S9: Water density profiles at the 80% graphene oxide interface, highlighting the effect of Lennard-Jones well depths (ϵ) on interfacial water aggregation, where ϵ represents carbon–water oxygen interactions. As ϵ increases, the water density peak becomes more pronounced, consistent with the trend reported in Supporting Note S11. For clarity, the computed discrete density is omitted, while continuous curves are generated using a Cubic Hermite interpolation.

References

[1] J. Tersoff, New empirical approach for the structure and energy of covalent systems, Physical Review B 37 (1988) 6991.

[2] H. Sun, COMPASS: An ab Initio Force-Field Optimized for Condensed-Phase Applications–Overview with Details on Alkane and Benzene Compounds, The Journal of Physical Chemistry B 102 (1998) 7338–7364.

[3] F. Jabbari, A. Rajabpour, S. Saedodin, S. Wongwises, Effect of water/carbon interaction strength on interfacial thermal resistance and the surrounding molecular nanolayer of cnt and graphene flake, Journal of Molecular Liquids 282 (2019) 197–204.

[4] V. Subasinghege Don, L. Kim, R. David, J. A. Nauman, R. Kumar, Adsorption studies at the graphene oxide–liquid interface: A molecular dynamics study, The Journal of Physical Chemistry C 127 (2023) 5920–5930.

[5] H. Yang, S. Gao, Y. Pan, P. Yang, Manipulating heat transfer at graphene/silicon interface with nitrogen doping, International Communications in Heat and Mass Transfer 155 (2024) 107521.

[6] A. Casto, M. Vittucci, F. Vialla, A. Crut, F. M. Bellussi, M. Fasano, F. Vallée, N. Del Fatti, F. Banfi, P. Maioli, Experimental optical retrieval of the thermal boundary resistance of carbon nanotubes in water, Carbon 229 (2024) 119445.

[7] D. Alexeev, J. Chen, J. H. Walther, K. P. Giapis, P. Angelikopoulos, P. Koumoutsakos, Kapitza resistance between few-layer graphene and water: liquid layering effects, Nano Letters 15 (2015) 5744–5749.

[8] S. Alosious, S. K. Kannam, S. P. Sathian, B. Todd, Kapitza resistance at water–graphene interfaces, The Journal of Chemical Physics 152 (2020) 224703.